

Monocular 3D Human Pose Estimation by Generation and Ordinal Ranking

Saurabh Sharma^{*1} Pavan Teja Varigonda² Prashast Bindal² Abhishek Sharma³ Arjun Jain²

¹Max Planck Institute for Informatics ²Indian Institute of Technology ³Gobasco AI Labs
Saarland Informatics Campus Bombay New Delhi

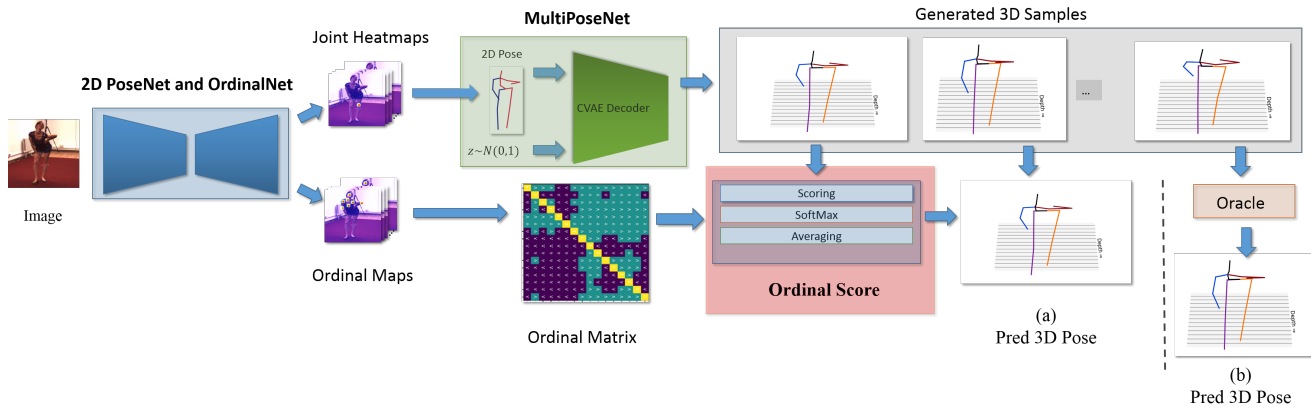


Figure 1: Our framework for monocular 3D Pose Estimation.

Abstract

*Monocular 3D Human Pose Estimation from static images is a challenging problem, due to the curse of dimensionality and the ill-posed nature of lifting 2D to 3D. In this paper, we propose a Deep Conditional Variational Autoencoder based model that synthesizes diverse 3D pose samples conditioned on the estimated 2D pose. Our experiments reveal that the CVAE generates significantly diverse 3D samples that are consistent with the 2D pose, thereby reducing the ambiguity in lifting from 2D-to-3D. We use two strategies for predicting the final 3D pose - (a) depth-ordering/ordinal relations to score and aggregate the final 3D pose, or *OrdinalScore*, and (b) with supervision from an *Oracle*. We report close to state of the art results on two benchmark datasets using *OrdinalScore*, and state-of-the-art results using the *Oracle*. We also show our pipeline gives competitive results without paired 3D supervision. We shall make the training and evaluation code available at https://github.com/ssfootball04/generative_pose.*

1. Introduction

Accurate 3D human-pose estimation from a monocular RGB image finds applications to robotics, virtual and aug-

mented reality, surveillance, pedestrian tracking, and human computer interaction. Its a hard problem to solve in real-world scenarios due to diverse variations in background, clothing, pose, occlusions, illumination, and camera parameters. Commonly used datasets such as Human3.6 [12], MPI-INF-3DHP [25], do not cover the entire range of these variations. Recent advancements in 2D human-pose estimation [28, 46] has led to several multi-stage architectures, where the 3D pose/body model is regressed either from both the image features and an intermediate 2D representation [49, 7, 3, 29], or only the estimated 2D pose [33, 1, 50, 24, 26]. However, none of these approaches explicitly tackle the ambiguity of lifting human-pose configuration from 2D to 3D, which is an inherently ill-posed problem. Motivated by this shortcoming, we propose to learn a generative model of 3D pose conditioned on 2D pose that allows us to model the 3D pose manifold and gives us the flexibility of drawing diverse 3D samples from it. To the best of our knowledge, we are the first to employ a Deep Conditional Variational Autoencoder [38] (CVAE for short) for 2D-to-3D generative human-pose modeling and demonstrate its advantages over direct regression based approaches. We also show that our generative 2D-to-3D mod-

^{*}Majority of this work was done while author was at Indian Institute of Technology, Bombay

ule can be trained using a MoCap data library, and still performs reasonably well on the unseen RGB images. Therefore, it is less dependent on image datasets with full 3D annotations, and robust to domain shift. Hence, our method can be trained in the most practical setting where annotating images with accurate 3D poses is often infeasible while 2D pose annotations of images and motion capture data can be collected separately without much effort [47].

Our pipeline is depicted in Figure 1. In the first stage, a deep convolutional network obtains a 2D pose estimate from a monocular RGB image. The estimated 2D pose and a latent code z , sampled from a prior $P(z) \sim \mathcal{N}(0, 1)$, are fed to the Decoder of the Conditional Variational Autoencoder to obtain a 3D pose. Multiple samples of z from $P(z)$ yield a diverse set of 3D pose samples that are consistent with the estimated 2D pose. We then use a joint-ordinal relation matrix that encodes the pairwise depth ordering of body-joints, extracted from another branch of the first stage CNN, to score the generated samples. These scores are finally fed to a Softmax operator to obtain a probability distribution over the obtained 3D sample set, and the predicted 3D pose is computed as the expectation of this distribution. In order to estimate the upper bound performance of our generative model, we also report results using an Oracle that gives us the best sample that minimises the error w.r.t the ground truth 3D pose. The obtained upper bound outperforms all existing state-of-the-art methods, without leveraging recently published annotated ordinal datasets, temporal information, or end-to-end training of the multi-stage architectures. This provides compelling evidence for the strength of our approach.

A summary of our contributions is as follows -

- We propose a learning based deep generative model that synthesizes diverse 3D pose samples conditioned on the estimated 2D pose, thereby reducing the ambiguity in lifting from 2D-to-3D.
- We show the application of a Deep Conditional Variational Autoencoder to 3D Human Pose Estimation for the first time.
- We obtain joint-ordinal relations from an RGB image and show their usage to rank 3D pose samples.
- Using an oracle, we report state-of-the-art results on two benchmark datasets, Human3.6M [12] and Human-Eva [35].
- We show that our 2D-to-3D module can perform reasonably well even when trained using a separate MoCap library *with no images!* Showing robustness to domain-shift and lack of image-3D datasets.

2. Related Work

Lifting 2D to 3D Our approach belongs to the large body of work that tries to obtain 3D pose from 2D joint locations. A linear combination based representation of human

3D pose on a sparse set of 3D bases, pre-trained using 3D mocap data[6], is shown in [33]. It was extended by [51] via convex relaxation to jointly estimate the coefficients of the sparse representation too. Anatomical constraints to regularize the predicted poses w.r.t. limb lengths were introduced in [44]. Further use of anatomical constraints in the form of joint-angle-limits and learned pose priors was proposed in [1] to extend [33]. In [26], Euclidean inter-joint distance matrix was used to represent 2D and 3D poses with multi-dimensional scaling to obtain 3D joint positions from the predicted 3D distance matrix. Some approaches, [3], estimate the 3D pose and shape by fitting a 3D statistical model [23] to 2D joint locations and leverage inter-penetration constraints. Different from all the previous approaches we employ CVAE to implicitly learn the anatomical constraints and sample probable candidate 3D poses.

The method in [14], builds upon the framework of [3] to describe a model that estimates the shape, underlying 3D pose and camera parameters using a re-projection and adversarial loss, which can be trained with 2d datasets and unpaired MoCap datasets. In [24], a baseline model is proposed that uses a simple fully connected linear network for this task which surprisingly outperforms past approaches. Unlike, these discriminative approaches that predict only one 3D pose we generate a diverse sample set of 3D poses.

Hypothesis Generation Some previous approaches sample multiple 3D poses via heuristics. The work in [22], finds the nearest neighbors in a learned latent embedding of human images to estimate the 3D pose. The approaches in [20] and [37], enumerate 3D poses using "kinematic-flipping" of the 3D joints, for estimation and tracking, respectively. The Bayesian framework from [36] employs a latent-variable generative model with a set of HOG-based 2D part detectors and performs inference using evolutionary algorithms. More recently, [4] retrieves 3D pose using nearest neighbor search. [13] uses the pose prior model of [1] to generate multiple hypothesis from a seed 3D pose, while [43] use "skeleton maps" at different scales to regress 3D pose hypothesis. Unlike the previous methods, our CVAE based generative model implicitly learns an anatomically consistent pose prior *conditioned* on the input 2D joint locations. It affords efficient sampling of a set of candidate 3D poses without requiring expensive MCMC or graphical model inference or an existing MoCap library. Also, it doesn't need additional image features or structural cues.

Ordinal Relations Ordinal relations have previously been explored to estimate depth [52, 5] and reflectance [48, 27]. Recently, [30] and [34] used 2D datasets with ordinal annotations as weak supervision for monocular 3D pose estimation by imposing a penalty for violation of ordinal depth constraints. Our ordinal prediction network is similar in spirit to [32] that uses a Structural-SVM conditioned on HOG features to predict pose-bits that capture qualitative at-

tributes to facilitate 3D pose prediction and image retrieval. Unlike [32], we employ more powerful fully convolutional network than HOG-based structured SVM, to jointly predict the 2D pose and depth-ordinal, which are further used to generate and score a diverse sample set of 3D poses. Concurrent with our work, [45] also predict depth ranking and regress 3D pose from 2D keypoints with depth rankings in a coarse-to-fine network.

Variational Autoencoders Variational Autoencoders have already shown promising results in generating many kinds of complicated data, including handwritten digits [17], faces [17], house numbers [16], CIFAR images [10], physical models of scenes [4], segmentation [7], and predicting the future from static images [42]. The recently proposed Conditional Variational Autoencoders ([38], [16]) additionally incorporate a conditioning variable, that allows to model multi-modal distributions for structured output problems. They have been used for object segmentation [38], future prediction [21], conditional appearance and shape generation [8], generating people in clothing [19], etc..

3. Proposed Approach

In this Section, we describe the various modules of our proposed approach. Sec. 3.1 introduces the notations used in this article followed by Sec. 3.2 that discusses 2DPoseNet to obtain 2D pose from an input RGB image. Sec. 3.3 describes our novel MultiPoseNet, a CVAE, for generating multiple 3D pose samples conditioned on the estimated 2D pose. In Sec. 3.4, we discuss OrdinalNet used to obtain joint-ordinal relations from the image. Finally, Sec. 3.5 and 3.6 describe our two strategies for predicting the final 3D pose : **(a)** by scoring the generated sample set using ordinal relations, referred to as OrdinalScore, and **(b)** by using supervision from an Oracle with access to the ground truth 3D pose, respectively.

3.1. Notations

We denote 3D human pose as an ordered set of 3D joint locations $J_{3D} = \{J_1, J_2, \dots, J_N\} \in R^{NX3}$, the corresponding 2D pose is denoted by J_{2D} . Probability distributions are written in capital boldface, \mathbf{X} , a random variable in lowercase italics, x and an observed sample in capital italics, X .

3.2. 2DPoseNet: 2D Joint-Locations from Image

We use the popular Stacked Hourglass Model [28] with two stacks to regress per-joint heatmaps (Gaussian bumps at target location). A tight 224×224 crop around the person resized to 224×224 , I , is fed to the Stacked Hourglass to obtain 16 heatmaps, H_i , of size 64×64 pixels, for each joint $J_i \in \{1, 2, \dots, 16\}$ in I . The 2D joint-locations are obtained as the maxima in each heatmap scaled back to the

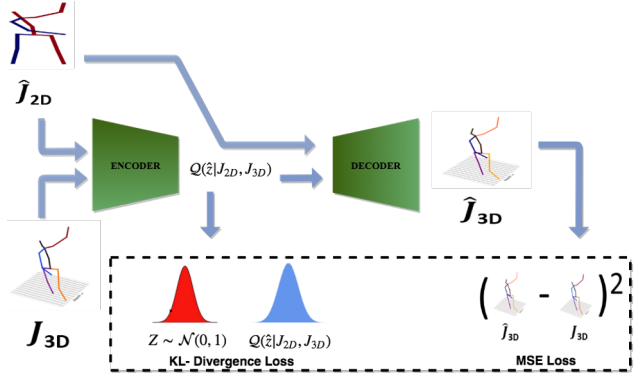


Figure 2: MultiPoseNet architecture at training time.

original image size to obtain estimated 2D pose \hat{J}_{2D} in pixel coordinates.

3.3. MultiPoseNet: Multiple 3D Poses from 2D

Recent success in generative modelling has shown that Variational Auto-encoders and Generative Adversarial Networks can estimate naturally occurring data distributions and synthesize realistic samples. Specially, CVAEs generate outputs conditioned on an input variable and are well suited for multi-modal regression mappings [38]. Therefore, we extend the baseline regression model from Martinez *et al* [24] into a CVAE to tackle the inherent multi-modality of the 2D-to-3D pose mapping and sample accurate and diverse 3D pose candidates conditioned on the estimated 2D pose \hat{J}_{2D} . The complete architecture for MultiPoseNet is depicted in Figure 2.

Training The 3D pose generating CVAE [38] consists of

- Recognition Network, or Encoder : $Enc(J_{3D}, J_{2D})$, which operates on an input 3D pose J_{3D} and a condition J_{2D} to output the mean and diagonal covariance for the posterior $q(\hat{z}|J_{3D}, J_{2D})$.
- Decoder : $Dec(\hat{z}, J_{2D})$, which reconstructs the ground truth J_{3D} by taking as input a latent \hat{z} sampled from the posterior $q(\hat{z}|J_{3D}, J_{2D})$ and the condition 2D pose J_{2D} .

During training, we optimize the following:

$$\begin{aligned} \mathcal{L}_{CVAE} = & KL(q(\hat{z}|J_{3D}, J_{2D})||p(z|J_{2D})) \\ & + \mathbb{E}_{q(\hat{z}|J_{3D}, J_{2D})} \|J_{3D} - Dec(\hat{z}, J_{2D})\|_2^2, \end{aligned} \quad (1)$$

where the prior distribution $p(z|J_{2D})$ is assumed to be $\mathcal{N}(0, 1)$, and $KL(x||y)$ is the Kullback-Leibler divergence. The expectation in the second term for the reconstruction loss is taken over K_{train} number of samples. In practise, we use two additional hyperparameters to assign weights to the KL and Reconstruction loss terms.

At inference time, the Encoder network is discarded, and z is drawn from the prior distribution, which is sub-optimal

because it makes the prediction and training pipelines inconsistent. To remedy this, we set the recognition network or Encoder equal to the prior network leading to a Gaussian Stochastic Neural Network, GSNN, proposed in [38]. Combining the two we get a hybrid training objective:

$$\mathcal{L}_{GSNN} = \mathbb{E}_{z \sim N(0,1)} \|J_{3D} - Dec(z, J_{2D})\|_2^2 \quad (2)$$

$$\mathcal{L}_{hybrid} = \alpha \mathcal{L}_{CVAE} + (1 - \alpha) \mathcal{L}_{GSNN}, \quad (3)$$

Inference We feed (z, \hat{J}_{2D}) to the Decoder, where $z \sim \mathcal{N}(0, 1)$ and \hat{J}_{2D} is the estimated 2D pose from the first stage, to get a diverse sample set $S = \{\hat{J}_{3D}^k: k \in \{1, 2, \dots, K_{test}\}\}$.

3.4. OrdinalNet: Image to Joint Ordinal Relations

The backbone architecture for OrdinalNet is same as our 2DPoseNet i.e. Stacked Hourglass [28] (SHGs). Specifically, we augment SHG with two additional stacks. For each joint $j \in \{1, 2, \dots, N\}$, three ordinal maps (OM_{1j} , OM_{2j} , and OM_{3j}) are predicted to capture the *lesser than*, *greater than* and *equal* depth relations between joint j and all other joints $i \in \{1, 2, \dots, N\}$. The ground-truth ordinal maps are generated so that for each joint j there is a Gaussian peak for joint $i \in \{1, 2, \dots, N\}$ in *one* of the three ordinal maps (OM_{1j} , OM_{2j} , and OM_{3j}), depending on the depth relation between joint i and joint j . We combine 2D pose heatmaps and intermediate feature representations from 2DPoseNet as the input, and use L2 loss over predicted ordinal maps for training our OrdinalNet. We regress for 48 (3×16) ordinal heat-maps, OM_{kj} , $k \in \{1, 2, 3\}$ and $j \in \{1, 2, \dots, 16\}$. OM_{1j} , OM_{2j} , and OM_{3j} maps correspond to the relations $J_j < J_i$, $J_j > J_i$ or $J_j \approx J_i$ respectively between joint j and all other joints $i \in \{1, 2, \dots, N\}$.

By applying non-maximal suppression on the predicted ordinal maps OM , and associating each peak to its nearest joint, we obtain our estimated ordinal relations, which are converted into a 16×16 joint-ordinal relation matrix \hat{M} . The relation between depths D_i, D_j of joints $i, j \in \{1, 2, \dots, N\}$ and ground truth matrix M is given by :

$$M_{ij} = \begin{cases} 1 & : D_i - D_j > 0 \\ 2 & : D_i - D_j < 0 \\ 3 & : D_i - D_j \approx 0 \end{cases}$$

3.5. OrdinalScore: Scoring and Aggregating Generated 3D samples

We use the estimated ordinal matrix \hat{M} to assign scores to each of the samples $J_{3D}^k \in S$ by the scoring function:

$$f(J_{3D}^k) = \Sigma(\hat{M} == g(J_{3D}^k)), \quad (4)$$

where $g(J_{3D}^k)$ is the function that computes the 16×16 ordinal matrix M for a 3D pose. To convert these scores into likelihood estimates, we pass the score through a Softmax

operator with temperature T to obtain a probability distribution over the candidate set. The final output \hat{J}_{3D} is the expectation over the candidates-

$$\hat{J}_{3D} = \Sigma \frac{(e^{Tf(J_{3D}^k)} J_{3D}^k)}{\Sigma e^{Tf(J_{3D}^k)}}, \quad (5)$$

The temperature based Softmax affords a fine control over the contribution strength of high-score samples vs. the low-scoring samples towards the final aggregation, which makes it robust to noisy pose candidates with respect to the predicted ordinal matrix M .

3.6. Supervision from an Oracle

The upper bound for our approach is given by choosing the best sample from the sample set S using an Oracle with access to the ground truth 3D pose J_{3D} . In this case, our final prediction is $\hat{J}_{3D} = Oracle(S, J_{3D})$.

4. Experiments

This section discusses the empirical evaluation of the proposed approach. First, we describe the benchmarks that we employed for quantitative and qualitative evaluation, and provide the important implementation details of our approach. Then, we present quantitative results and compare our method with the state-of-the-art, and provide ablative studies to analyze the performance of our generative model.

4.1. Datasets

We make use of the following datasets for training various modules of our pipeline :

CMU Mocap motion capture dataset consists of diverse 3D poses with 144 different subjects performing different actions. We obtain 2D projections from the 3D skeletons using virtual cameras from multiple views, with assumed intrinsic parameters. We use obtained 2D-3D pose data for training MultiPoseNet and the baseline model from [24] for our unpaired setting experiments, where we train our networks without using any Image-3D data.

Human3.6M dataset consists of 3.6 million 3D human poses. It consists of videos and MoCap data of 5 female and 6 male subjects, captured from 4 different viewpoints while they are performing typical activities (talking on the phone, walking, greeting, eating, etc.).

HumanEva-I is a small dataset containing 3 subjects (S1, S2, S3) with 3 camera views and fewer actions than Human3.6M. This is a standard dataset for 3D pose estimation used for benchmarking in previous works.

4.2. Implementation Details

Data Pre-processing Following [24], we process the 3D joint position in camera coordinates and apply standard normalization to the 2d inputs and 3d outputs by subtracting

the mean and dividing by the standard deviation, and zero-center the 3d poses around the hip joint. The 2D and 3D poses have $N=16$ and $N=17$ joints respectively.

2DPoseNet: We take publicly available Stacked Hourglass pretrained on MPII [2] as our base 2DPoseNet and fine-tune our model on Human3.6M following [24].

MultiPoseNet: The MultiPoseNet architecture is based on the baseline model in [24]. Exact network details can be found in the supplementary material. At training time, the expectation in 1 is estimated using $K_{train} = 10$ samples. KL and reconstruction loss weights are set to 10 and 100 respectively. The network is trained for 200 epochs using Adam [15], starting with a learning rate of 2.5e-4 with exponential decay, mini-batches size of 256. At test time, we generate $K_{test} = 200$ 3D pose candidates to get a diverse sample set S . MultiPoseNet takes 10 hours to train on a Titan 1080ti GPU.

OrdinalNet We integrate the 2DPoseNet pretrained on MPII and Human3.6M with a Stacked-Hourglass module containing 2 stacks for predicting ordinal maps M . We train the OrdinalNet Hourglass module using ground-truth ordinal maps from Human3.6M for 60 epochs with standard L2 Loss while freezing the weights of 2DPoseNet. OrdinalNet takes 12 hours to train, on a Titan 1080ti GPU.

OrdinalScore The temperature, T , is obtained using cross-validation and set to 0.9 for ground truth ordinals, and 0.3 for predicted ordinals. In practise, OrdinalNet can predict sometimes contradictory relations i.e $\hat{M}_{ij} \neq \hat{M}_{ji}$, $\hat{M}_{ii} \neq 3$; to account for this we always set the diagonal entries of M to 3 and mask out elements where $\hat{M}_{ij} \neq \hat{M}_{ji}$ during scoring.

Runtime Details The run-time for different modules of our pipeline are - *OrdinalNet*: 20ms/image, *MultiPoseNet*: 0.5ms/sample, we take 200 samples/image for inference. The entire pipeline runs at 10 fps on a commodity graphics card, which is slightly worse than other real-time methods.

4.3. Quantitative Evaluation

In this section we report the results of our model and compare it against the prior state-of-the-art on Human3.6M and HumanEva-I dataset. We report three evaluation metrics to show the performance gains of our approach :

PRED Ordinals : Uses the OrdinalScore strategy with the ordinal relations predicted by OrdinalNet.

GT Ordinals : Uses the OrdinalScore strategy with the ground truth ordinal relations.

Oracle : Uses the Oracle for final prediction, which gives the best results.

4.3.1 Evaluation on Human3.6M

Following the literature, we follow two standard protocols to train and evaluate our results.

In *Protocol 1*, the training set consists of 5 subjects (S1, S5, S6, S7, S8), while the test set includes 2 subjects (S9,

S11). The original frame rate of 50 FPS is down-sampled to 10 FPS and the evaluation is on sequences coming from all 4 cameras and all trials. The reported error metric is Mean Per Joint Position Error (MPJPE) i.e. the Euclidean distance from the estimated 3D joints to the ground truth, averaged over 17 joints of the Human3.6M skeletal model.

For *Protocol 2*, Subjects S1, S5, S6, S7, S8 and S9 are used for training and the testing is performed on subject S11. The error metric used is Procrustes Aligned MPJPE (PA MPJPE) which is the MPJPE calculated after rigidly aligning the predicted pose with the ground truth.

Table 1 and Table 2 show our results for Protocol 1 and Protocol 2, respectively. In the paired setting, we make use of 3D pose annotations from Human3.6M and train both our networks using this dataset. We outperform all existing methods using Oracle supervision, although it is a slightly unfair comparison. Using GT ordinals we also outperform almost all other approaches, and with PRED Ordinals our performance is competitive but not state-of-the-art. Note that here we are worse only to methods that either use additional ordinal training data [30], temporal information [7, 11] and/or soft-argmax [40] (denoted by *s), all of which is compatible with our approach.

Without Paired 3D Supervision The 2D-to-3D lifting module of our pipeline can be trained using a separate MoCap library, therefore lacking access to paired image-to-3D correspondence. To demonstrate this, we train MultiPoseNet on the CMU MoCap dataset, which consists of only 3D MoCap data, and report the results on the test set of Human3.6M. Note that the MoCap dataset is required for training, and not during inference. The 3D poses from CMU MoCap are virtually projected to their corresponding 2D key-points, by fixing the camera at the origin and translating the root joint, pelvis, to a distance of 5500mm. The intrinsic camera parameters depend only on the focal length, which is taken from one of the cameras of Human3.6M, to bring the distribution of 2D projections closer to the Human3.6 test set. We also rotate the 3D poses by 90, 180, and 270 degrees, for data augmentation. We train the baseline model [24] and MultiPoseNet on this dataset, and test on the estimated 2D poses and ordinals from 2DPoseNet and OrdinalNet, which are trained using 2D pose and ordinal data from Human3.6M. Note that Human3.6 data is used only for 2D pose and ordinal estimation, therefore we are not exploiting any image-3D data annotations. As we use two different sources for the image-2d/ordinal and 2d-3d modules, we refer to this as the unpaired setting. The results of these experiments are reported in Table 1 and 2 in the bottom rows.

Our method yields very competitive results, given the challenging nature of the setting. The trends are similar, the Oracle estimate is the best followed by GT Ordinals and PRED Ordinals respectively. We also comfortably outper-

| Protocol 1 | Direct. | Discuss | Eating | Greet | Phone | Photo | Pose | Purch. | Sitting | SitingD | Smoke | Wait | WalkD | Walk | WalkT | Avg | |
|------------|------------------------------|---------|--------|-------|-------|-------|---------|--------|---------|---------|-------|-------|-------|-------|-------|-------|-------|
| PAIR | Pavlakos <i>et al.</i> [31] | 67.4 | 71.9 | 66.7 | 69.1 | 72.0 | 77.0 | 65.0 | 68.3 | 83.7 | 96.5 | 71.7 | 65.8 | 74.9 | 59.1 | 63.2 | 71.9 |
| | Zhou <i>et al.</i> [49] | 54.82 | 60.70 | 58.22 | 71.4 | 62.0 | 65.5 | 53.8 | 55.6 | 75.2 | 111.6 | 64.1 | 66.0 | 51.4 | 63.2 | 55.3 | 64.9 |
| | Martinez <i>et al.</i> [24] | 51.8 | 56.2 | 58.1 | 59.0 | 69.5 | 78.4 | 55.2 | 58.1 | 74.0 | 94.6 | 62.3 | 59.1 | 65.1 | 49.5 | 52.4 | 62.9 |
| | Sun <i>et al.</i> [39] | 52.8 | 54.8 | 54.2 | 54.3 | 61.8 | 67.2 | 53.1 | 53.6 | 71.7 | 86.7 | 61.5 | 53.4 | 61.6 | 47.1 | 53.4 | 59.1 |
| | Fang <i>et al.</i> [9] | 50.1 | 54.3 | 57.0 | 57.1 | 66.6 | 73.3 | 53.4 | 55.7 | 72.8 | 88.6 | 60.3 | 57.7 | 62.7 | 47.5 | 50.6 | 60.4 |
| | *Pavlakos <i>et al.</i> [30] | 48.5 | 54.4 | 54.4 | 52.0 | 59.4 | 65.3 | 49.9 | 52.9 | 65.8 | 71.1 | 56.6 | 52.9 | 60.9 | 44.7 | 47.8 | 56.2 |
| | **Hossain <i>et al.</i> [11] | 44.2 | 46.7 | 52.3 | 49.3 | 59.9 | 59.4 | 47.5 | 46.2 | 59.9 | 65.6 | 55.8 | 50.4 | 52.3 | 43.5 | 45.1 | 51.9 |
| | **Dabral <i>et al.</i> [7] | 44.8 | 50.4 | 44.7 | 49.0 | 52.9 | 61.4 | 43.5 | 45.5 | 63.1 | 87.3 | 51.7 | 48.5 | 37.6 | 52.2 | 41.9 | 52.1 |
| | ***Sun <i>et al.</i> [40] | 47.5 | 47.7 | 49.5 | 50.2 | 51.4 | 43.8 | 46.4 | 58.9 | 65.7 | 49.4 | 55.8 | 47.8 | 38.9 | 49.0 | 43.8 | 49.6 |
| | Ours (PRED Ordinals) | 48.6 | 54.5 | 54.2 | 55.7 | 62.6 | 72.0 | 50.5 | 54.3 | 70.0 | 78.3 | 58.1 | 55.4 | 61.4 | 45.2 | 49.7 | 58.0 |
| UNPAIR | Ours (GT Ordinals) | 42.9 | 48.1 | 47.8 | 50.2 | 56.1 | 65.0 | 44.9 | 48.6 | 61.8 | 69.9 | 52.6 | 50.4 | 56.0 | 42.1 | 45.1 | 52.1 |
| | Ours (With Oracle) | 37.8 | 43.2 | 43.0 | 44.3 | 51.1 | 57.0 | 39.7 | 43.0 | 56.3 | 64.0 | 48.1 | 45.4 | 50.4 | 37.9 | 39.9 | 46.8 |
| | Martinez <i>et al.</i> [24] | 109.9 | 112 | 103.8 | 115.3 | 119.3 | 119.3 | 114 | 116.6 | 118.9 | 127.3 | 112.2 | 119.8 | 113.4 | 119.8 | 111.9 | 115.6 |
| UNPAIR | Ours (PRED Ordinals) | 99.9 | 102.7 | 97.9 | 105.9 | 112.0 | 111.7 | 103.9 | 109.4 | 111.7 | 119.4 | 104.8 | 110.8 | 103.2 | 106.9 | 102.3 | 106.8 |
| | Ours (GT Ordinals) | 97.9 | 100.5 | 95.4 | 103.7 | 109.4 | 108.5 | 102.0 | 108.0 | 107.9 | 115.4 | 102.2 | 108.9 | 100.8 | 105.8 | 100.8 | 104.4 |
| | Ours (With Oracle) | 92.6 | 94.6 | 90.6 | 98.4 | 103.8 | 103.3.6 | 96.6 | 101.8 | 101.7 | 108.8 | 96.6 | 102.7 | 95.3 | 100.6 | 96.1 | 98.9 |

Table 1: Detailed results on Human3.6M under Protocol 1 (no rigid alignment in post-processing). Error is in millimeters(mm). Top: Paired methods (PAIR), Bottom: unpaired methods (UNPAIR). Results for [24] in the unpaired setting were obtained using their publicly available code. * - use additional ordinal training data from MPII and LSP. ** - use temporal information. *** - use soft-argmax for end-to-end training. These strategies are complementary with our approach.

| Protocol 2 | Direct. | Discuss | Eating | Greet | Phone | Photo | Pose | Purch. | Sitting | SitingD | Smoke | Wait | WalkD | Walk | WalkT | Avg | |
|------------|------------------------------|---------|--------|-------|-------|-------|------|--------|---------|---------|-------|------|-------|------|-------|------|------|
| PAIR | Zhou <i>et al.</i> [49] | 47.9 | 48.8 | 52.7 | 55.0 | 56.8 | 49.0 | 45.5 | 60.8 | 81.1 | 53.7 | 65.5 | 51.6 | 50.4 | 54.8 | 55.9 | 55.3 |
| | Pavlakos <i>et al.</i> [31] | 47.5 | 50.5 | 48.3 | 49.3 | 50.7 | 55.2 | 46.1 | 48.0 | 61.1 | 78.1 | 51.1 | 48.3 | 52.9 | 41.5 | 46.4 | 51.9 |
| | Martinez <i>et al.</i> [24] | 39.5 | 43.2 | 46.4 | 47.0 | 51.0 | 56.0 | 41.4 | 40.6 | 56.5 | 69.4 | 49.2 | 45.0 | 49.5 | 38.0 | 43.1 | 47.7 |
| | Fang <i>et al.</i> [9] | 38.2 | 41.7 | 43.8 | 44.9 | 48.5 | 55.3 | 40.2 | 38.2 | 54.5 | 64.4 | 47.2 | 44.3 | 47.3 | 36.7 | 41.7 | 45.7 |
| | Sun <i>et al.</i> [39] | 42.1 | 44.3 | 45.0 | 45.4 | 51.5 | 53.0 | 43.2 | 41.3 | 59.3 | 73.3 | 51.0 | 44.0 | 48.0 | 38.3 | 44.8 | 48.3 |
| | *Pavlakos <i>et al.</i> [30] | 34.7 | 39.8 | 41.8 | 38.6 | 42.5 | 47.5 | 38.0 | 36.6 | 50.7 | 56.8 | 42.6 | 39.6 | 43.9 | 32.1 | 36.5 | 41.8 |
| | **Hossain <i>et al.</i> [11] | 36.9 | 37.9 | 42.8 | 40.3 | 46.8 | 46.7 | 37.7 | 36.5 | 48.9 | 52.6 | 45.6 | 39.6 | 43.5 | 35.2 | 38.5 | 42.0 |
| | **Dabral <i>et al.</i> [7] | 28.0 | 30.7 | 39.1 | 34.4 | 37.1 | 44.8 | 28.9 | 31.2 | 39.3 | 60.6 | 39.3 | 31.1 | 25.3 | 37.8 | 28.4 | 36.3 |
| | ***Sun <i>et al.</i> [40] | - | - | - | - | - | - | - | - | - | - | - | - | - | - | - | 40.6 |
| | Ours (PRED Ordinals) | 35.3 | 35.9 | 45.8 | 42.0 | 40.9 | 52.6 | 36.9 | 35.8 | 43.5 | 51.9 | 44.3 | 38.8 | 45.5 | 29.4 | 34.3 | 40.9 |
| UNPAIR | Ours (GT Ordinals) | 31.3 | 31.0 | 39.3 | 37.0 | 37.2 | 47.8 | 32.5 | 32.1 | 39.8 | 47.3 | 40.0 | 34.7 | 41.8 | 27.5 | 31.0 | 36.7 |
| | Ours (With Oracle) | 27.6 | 27.5 | 34.9 | 32.3 | 33.3 | 42.7 | 28.7 | 28.0 | 36.1 | 42.7 | 36.0 | 30.7 | 37.6 | 24.3 | 27.1 | 32.7 |
| | Martinez <i>et al.</i> [24] | 62.6 | 64.3 | 62.5 | 67.4 | 72.2 | 70.8 | 64.9 | 61.2 | 82.1 | 92.4 | 76.8 | 66.7 | 71.7 | 79.5 | 73.1 | 71.3 |
| | Ours (PRED Ordinals) | 62.9 | 65.6 | 61.8 | 67.1 | 72.2 | 69.3 | 65.6 | 63.8 | 81.3 | 91.0 | 74.5 | 66.5 | 70.8 | 74.7 | 70.9 | 70.5 |
| UNPAIR | Ours (GT Ordinals) | 62.9 | 65.3 | 60.7 | 66.9 | 71.3 | 68.4 | 65.2 | 63.2 | 80.1 | 89.3 | 73.5 | 66.1 | 70.5 | 74.7 | 70.9 | 70.0 |
| | Ours (With Oracle) | 56.8 | 59.2 | 55.0 | 59.6 | 65.6 | 62.0 | 58.4 | 56.5 | 74.2 | 82.8 | 67.6 | 60.0 | 63.6 | 68.2 | 64.3 | 63.6 |

Table 2: Detailed results on Human3.6M under Protocol 2 (rigid alignment in post-processing). Top: Paired methods (PAIR), Bottom: unpaired methods (UNPAIR). Results for [24] in the unpaired setting were obtained using their publicly available code.

form the baseline regression model [24] using all three estimates. Our framework is therefore less dependent on image datasets with full 3D annotations, and robust to domain shift.

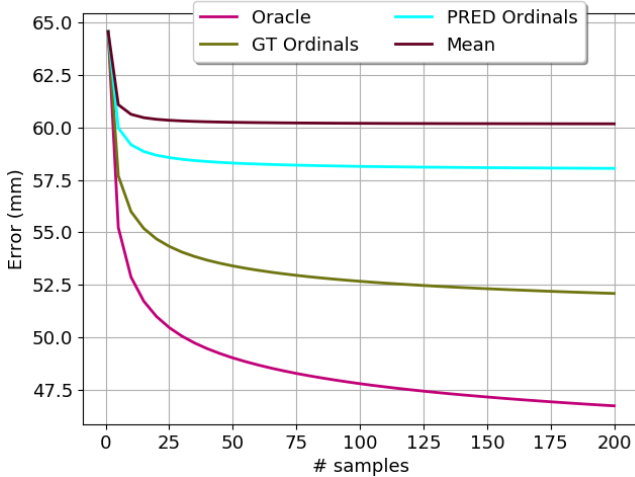
4.3.2 Evaluation on HumanEva-I

Following the standard protocol outlined in [18], we evaluated our model on HumanEva-I. Training is done on subjects S1, S2, S3 under different view-points only for action-sequences *Jogging* and *Walking* and evaluation of our model is done on the validation sequences for all three subjects as testing data. We report the model error using reconstruction error after rigid transformation. All of our networks are trained using HumanEva-I in this setting. We obtain state-of-the-art results using the Oracle estimate and

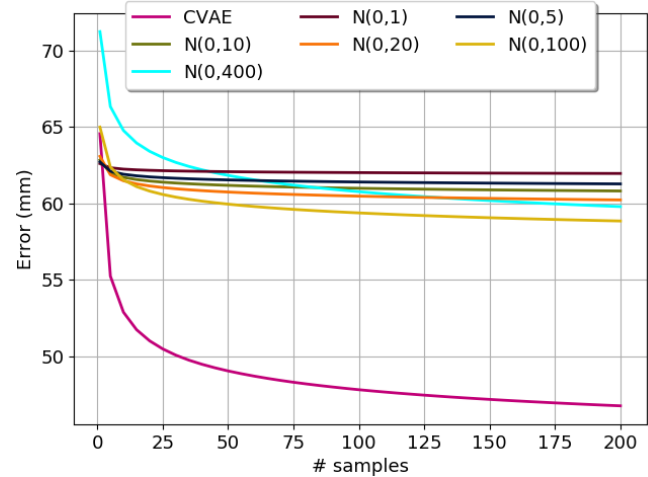
close to state-of-the-art with OrdinalScore on HumanEva-I in Table 3.

| | Jogging | | | Walking | | | Avg |
|----------------------------------|---------|------|------|---------|------|------|------|
| | S1 | S2 | S3 | S1 | S2 | S3 | |
| Kostrikov <i>et al.</i> [18] | 44.0 | 30.9 | 41.7 | 57.2 | 35.0 | 33.3 | 40.3 |
| Yasin <i>et al.</i> [47] | 35.8 | 32.4 | 41.6 | 46.6 | 41.4 | 35.4 | 38.9 |
| Moreno-Noguer <i>et al.</i> [26] | 19.7 | 13.0 | 24.9 | 39.7 | 20.0 | 21.0 | 26.9 |
| Pavlakos <i>et al.</i> [31] | 22.1 | 21.9 | 29.0 | 29.8 | 23.6 | 26.0 | 25.5 |
| Martinez <i>et al.</i> [24] | 19.7 | 17.4 | 46.8 | 26.9 | 18.2 | 18.6 | 24.6 |
| Ours (PRED Ordinals) | 19.3 | 12.5 | 41.8 | 40.9 | 22.1 | 18.6 | 25.9 |
| Ours (GT Ordinals) | 19.1 | 12.4 | 41.5 | 40.6 | 21.9 | 18.5 | 25.7 |
| Ours (With Oracle) | 17.4 | 11.0 | 39.5 | 38.5 | 20.1 | 16.7 | 23.9 |

Table 3: Results of our model on HumanEva-I dataset and a comparison with previous work. Numbers reported are mean reconstruction error in mm computed after rigid transformation.



(a) Oracle vs OrdinalScore



(b) CVAE vs Naive sampling

Figure 3: Ablation studies. (a) Effect of increasing number of samples on OrdinalScore and Oracle estimate (b) Comparison of CVAE versus simple baseline sampling with access to an oracle.

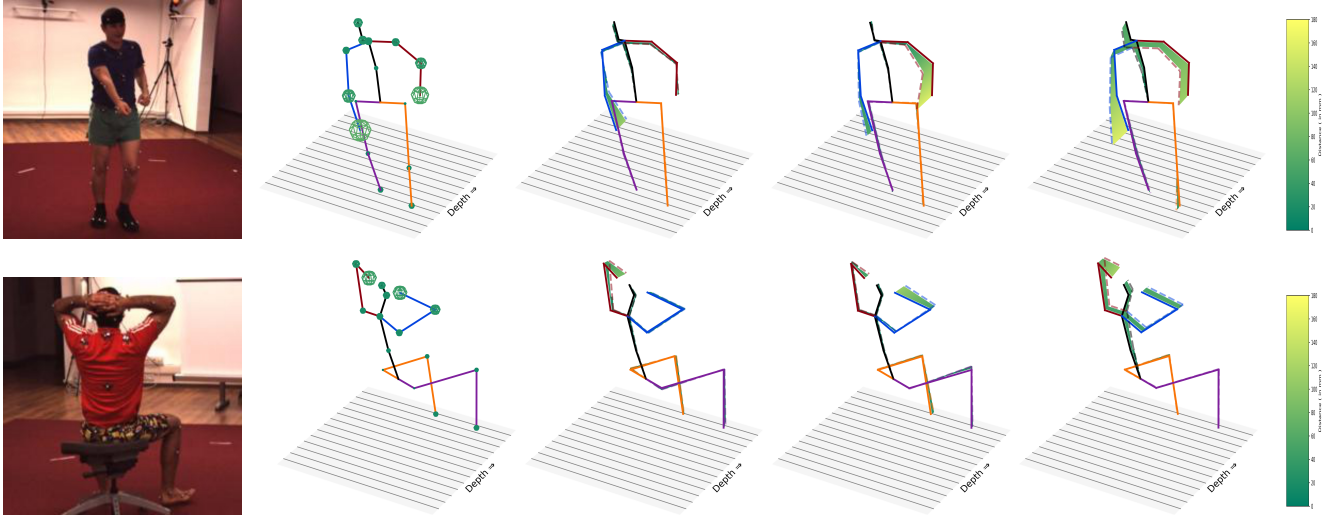


Figure 4: Sample diversity on the Human3.6 dataset. From left to right : (1) Input Image (2) Mean Pose with standard deviation around each joint. (3) Three different samples overlaid on top of mean pose. Mean is solid and sample is dashed, with displacement vector field in between. Note that the wrist and elbow show maximum variance, as expected.

4.4. OrdinalNet Accuracy

We report the accuracy of our *OrdinalNet* by comparing the ground truth M ordinal matrix with the predicted \hat{M} ordinal matrix. The results on the validation set for Human3.6M and HumanEva-I are 86.8% and 81% respectively.

4.5. Ablation Studies

Effect of Increasing Number of Samples In this ablation we study the effect of increasing number of samples on our error estimate. In Figure 3, we plot the value of different error estimates on Protocol 1 of Human3.6 as we increase the

number of samples. Mean denotes the simple mean of all samples, others have the same meaning as before. We make several important observations. Firstly, the mean value improves its estimates with increasing number of samples, but saturates quickly. The curve for the best sample estimate indicates that the chances of obtaining a good pose candidate increases as we sample more. Consequently, the expectation obtained using ordinal scoring improves its estimate, as we observe from the curves for predicted and ground truth ordinals, which also decrease with increasing samples. This also demonstrates that ordinal scoring is an effective strategy for assigning probability estimates to the generated samples.

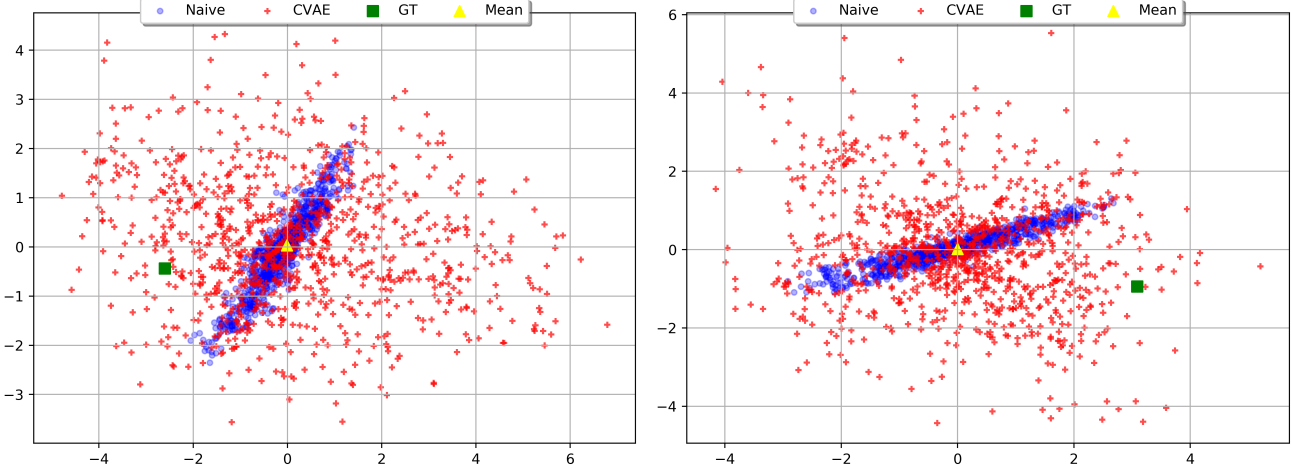


Figure 5: Samples from CVAE and baseline (using a variance of 100) mapped to a Euclidean space using ISOMAP [41]. Note that CVAE produces much more diverse samples that are likely to be near the GT pose.

Sampling Baseline - In this ablation, we study a simple sampling baseline coupled with an Oracle. For this experiment, we fit marginal Gaussians at each joint and sample independently from each marginal distribution to get a 3D pose sample. We take the mean from the baseline regression model, and variance belonging to [1,5,10,20,100,400]. Figure 3 shows the comparison of MultiPoseNet with this simple baseline for the Oracle estimate on Protocol 1 of Human3.6 as we increase the number of samples. From the plot, it is clear that the baseline has a very poor gradient and can only improve upon the point estimate by 2mm, even sampling at a very high variance of 100mm. The baseline performance begins to deteriorate with variances higher than 400mm as the samples become meaningless. Contrastingly, MultiPoseNet improves its estimate by close to 20mm and the gradient of its curve indicates the performance can improve by sampling further.

4.6. Sample Diversity

Qualitative Analysis The major motivation behind using a generative model for 2D-to-3D lifting was to generate a diverse set of plausible 3D pose candidates for the given 2D pose. Therefore, it is important to assess the diversity present in the generated candidate set. We show the mean pose, per joint standard deviation, and a few candidate 3D poses for two different images in Figure 4. The visualization shows we generate meaningful variations across different body parts and poses. Also note that the standard deviation is particularly high around the wrist and elbow joints, which are the hardest to predict, which is as we would expect.

Visualisation Using Dimensionality Reduction To understand the distribution of generated samples, we map samples from MultiPoseNet and the simple baseline (using a

variance of 100) to a Euclidean space using a dimensionality reduction technique that focuses on global structure [41]. In Figure 5, we sample 1000 times from both models and visualise them for two different condition 2D poses, along with the ground truth 3D pose and the mean estimate of the CVAE. The results are quite interesting. The samples from the baseline cluster in a narrow space around the mean, whereas the samples generated by the CVAE are very diverse and are likely to end up near the GT 3D pose even when it is far from the mean point estimate of the model.

5. Conclusions and Future Work

In this paper, we presented a novel framework for monocular 3D pose estimation that uses a convolutional variational autoencoder for sampling 3D candidates, and ranks and computes an expectation over the sample set using ordinal relations that our predicted from a convolutional neural network. Our method achieves close to state-of-the-art results on two benchmark datasets using OrdinalScore, and state-of-the-results using an Oracle with access to the ground truth 3D pose. Our experiments demonstrate that a CVAE can learn a generate model that synthesize diverse 3D samples consistent with the 2D pose, thereby reducing the ambiguity in lifting from 2D-to-3D. We also showed our model can be trained without paired 3D supervision and still yield competitive results.

In future research, we shall extend our sampling mechanism to videos where temporal cues can further improve sample likelihood estimation.

References

- [1] I. Akhter and M. J. Black. Pose-conditioned joint angle limits for 3d human pose reconstruction. In *CVPR*, 2015.

2

[2] M. Andriluka, L. Pishchulin, P. Gehler, and B. Schiele. 2d human pose estimation: New benchmark and state of the art analysis. In *CVPR*, 2014. 5

[3] F. Bogo, A. Kanazawa, C. Lassner, P. Gehler, J. Romero, and M. J. Black. Keep it smpl: Automatic estimation of 3d human pose and shape from a single image. In *ECCV*, 2016. 1, 2

[4] C.-H. Chen and D. Ramanan. 3d human pose estimation = 2d pose estimation + matching. In *CVPR*, 2017. 2

[5] W. Chen, Z. Fu, D. Yang, and J. Deng. Single-image depth perception in the wild. In *NIPS*, 2016. 2

[6] CMU. Carnegie mellon university graphics lab - motion capture library, 2014. <http://mocap.cs.cmu.edu/>. 2

[7] R. Dabral, A. Mundhada, U. Kusupati, S. Afaque, A. Sharma, and A. Jain. Learning 3d human pose from structure and motion. In *ECCV*, 2018. 1, 5, 6

[8] P. Esser, E. Sutter, and B. Ommer. A variational u-net for conditional appearance and shape generation. In *CVPR*, 2018. 3

[9] H. Fang, Y. Xu, W. Wang, X. Liu, and S. Zhu. Learning pose grammar to encode human body configuration for 3d pose estimation. In *AAAI*, 2018. 6

[10] K. Gregor, I. Danihelka, A. Graves, D. J. Rezende, and D. Wierstra. Draw: a recurrent neural network for image generation. In *ICML*, 2015. 3

[11] M. R. I. Hossain and J. J. Little. Exploiting temporal information for 3d human pose estimation. In *ECCV*, 2018. 5, 6

[12] C. Ionescu, D. Papava, V. Olaru, and C. Sminchisescu. Human3.6m: Large scale datasets and predictive methods for 3d human sensing in natural environments. *PAMI*, 2014. 1, 2

[13] E. Jahangiri and A. L. Yuille. Generating multiple diverse hypotheses for human 3d pose consistent with 2d joint detections. In *ICCV*, 2017. 2

[14] A. Kanazawa, M. J. Black, D. W. Jacobs, and J. Malik. End-to-end recovery of human shape and pose. In *CVPR*, 2018. 2

[15] D. P. Kingma and J. Ba. Adam: A method for stochastic optimization. In *ICLR*, 2015. 5

[16] D. P. Kingma, S. Mohamed, D. J. Rezende, and M. Welling. Semi-supervised learning with deep generative models. In *NIPS*, 2014. 3

[17] D. P. Kingma and M. Welling. Auto-encoding variational bayes. *ICLR*, 2013. 3

[18] I. Kostrikov and J. Gall. Depth sweep regression forests for estimating 3d human pose from images. In *BMVC*, 2014. 6

[19] C. Lassner, G. Pons-Moll, and P. V. Gehler. A generative model of people in clothing. In *ICCV*, 2017. 3

[20] M. W. Lee and I. Cohen. Proposal maps driven mcmc for estimating human body pose in static images. In *CVPR*, 2004. 2

[21] N. Lee, W. Choi, P. Vernaza, C. B. Choy, P. H. Torr, and M. Chandraker. Desire: Distant future prediction in dynamic scenes with interacting agents. In *CVPR*, 2017. 3

[22] S. Li, W. Zhang, and A. B. Chan. Maximum-margin structured learning with deep networks for 3d human pose estimation. In *ICCV*, 2015. 2

[23] M. Loper, N. Mahmood, J. Romero, G. Pons-Moll, and M. J. Black. Smpl: A skinned multi-person linear model. *ACM transactions on graphics (TOG)*, 2015. 2

[24] J. Martinez, R. Hossain, J. Romero, and J. J. Little. A simple yet effective baseline for 3d human pose estimation. In *ICCV*, 2017. 1, 2, 3, 4, 5, 6

[25] D. Mehta, H. Rhodin, D. Casas, P. Fua, O. Sotnychenko, W. Xu, and C. Theobalt. Monocular 3d human pose estimation in the wild using improved cnn supervision. In *3DV*, 2017. 1

[26] F. Moreno-Noguer. 3d human pose estimation from a single image via distance matrix regression. In *CVPR*, 2017. 1, 2, 6

[27] T. Narihira, M. Maire, and S. X. Yu. Learning lightness from human judgement on relative reflectance. In *CVPR*, 2015. 2

[28] A. Newell, K. Yang, and J. Deng. Stacked hourglass networks for human pose estimation. In *ECCV*, 2016. 1, 3, 4

[29] M. Omran, C. Lassner, G. Pons-Moll, P. Gehler, and B. Schiele. Neural body fitting: Unifying deep learning and model based human pose and shape estimation. In *3DV*, 2018. 1

[30] G. Pavlakos, X. Zhou, and K. Daniilidis. Ordinal depth supervision for 3d human pose estimation. In *CVPR*, 2018. 2, 5, 6

[31] G. Pavlakos, X. Zhou, K. G. Derpanis, and K. Daniilidis. Coarse-to-fine volumetric prediction for single-image 3d human pose. In *CVPR*, 2017. 6

[32] G. Pons-Moll, D. J. Fleet, and B. Rosenhahn. Posebits for monocular human pose estimation. In *CVPR*, 2014. 2, 3

[33] V. Ramakrishna, T. Kanade, and Y. Sheikh. Reconstructing 3d human pose from 2d image landmarks. In *ECCV*, 2012. 1, 2

[34] M. R. Ronchi, O. Mac Aodha, R. Eng, and P. Perona. It's all relative: Monocular 3d human pose estimation from weakly supervised data. *BMVC*, 2018. 2

[35] L. Sigal, A. O. Balan, and M. J. Black. Humaneva: Synchronized video and motion capture dataset and baseline algorithm for evaluation of articulated human motion. *International journal of computer vision*, 2010. 2

[36] E. Simo-Serra, A. Quattoni, C. Torras, and F. Moreno-Noguer. A joint model for 2d and 3d pose estimation from a single image. In *CVPR*, 2013. 2

[37] C. Sminchisescu and B. Triggs. Kinematic jump processes for monocular 3d human tracking. In *CVPR*, 2003. 2

[38] K. Sohn, H. Lee, and X. Yan. Learning structured output representation using deep conditional generative models. In *NIPS*, 2015. 1, 3, 4

[39] X. Sun, J. Shang, S. Liang, and Y. Wei. Compositional human pose regression. In *ICCV*, 2017. 6

[40] X. Sun, B. Xiao, F. Wei, S. Liang, and Y. Wei. Integral human pose regression. In *ECCV*, 2018. 5, 6

[41] J. B. Tenenbaum, V. De Silva, and J. C. Langford. A global geometric framework for nonlinear dimensionality reduction. *Science*, 2000. 8

- [42] J. Walker, C. Doersch, A. Gupta, and M. Hebert. An uncertain future: Forecasting from static images using variational autoencoders. In *ECCV*. Springer, 2016. 3
- [43] Q. Wan, W. Zhang, and X. Xue. DeepSkeleton: Skeleton map for 3d human pose regression. *arXiv preprint arXiv:1711.10796*, 2017. 2
- [44] C. Wang, Y. Wang, Z. Lin, A. L. Yuille, and W. Gao. Robust estimation of 3d human poses from a single image. In *CVPR*, 2014. 2
- [45] M. Wang, X. Chen, W. Liu, C. Qian, L. Lin, and L. Ma. Drpose3d: Depth ranking in 3d human pose estimation. *IJCAI*, 2018. 3
- [46] S.-E. Wei, V. Ramakrishna, T. Kanade, and Y. Sheikh. Convolutional pose machines. In *CVPR*, 2016. 1
- [47] H. Yasin, U. Iqbal, B. Kruger, A. Weber, and J. Gall. A dual-source approach for 3d pose estimation from a single image. In *CVPR*, 2016. 2, 6
- [48] T. Zhou, P. Krahenbuhl, and A. A. Efros. Learning data-driven reflectance priors for intrinsic image decomposition. In *ICCV*, 2015. 2
- [49] X. Zhou, Q. Huang, X. Sun, X. Xue, and Y. Wei. Towards 3d human pose estimation in the wild: A weakly-supervised approach. In *ICCV*, 2017. 1, 6
- [50] X. Zhou, M. Zhu, K. Derpanis, and K. Daniilidis. Sparseness meets deepness: 3d human pose estimation from monocular video. In *CVPR*, 2016. 1
- [51] X. Zhou, M. Zhu, S. Leonardos, and K. Daniilidis. Sparse representation for 3d shape estimation: A convex relaxation approach. *PAMI*. 2
- [52] D. Zoran, P. Isola, D. Krishnan, and W. T. Freeman. Learning ordinal relationships for mid-level vision. In *ICCV*, 2015. 2